



**HAL**  
open science

## Structure of the 001 talc surface as seen by atomic force microscopy: Comparison with X-ray and electron diffraction results

Eric Ferrage, Grégory Seine, Anne-Claire Gaillot, Sabine Petit, Philippe de Parseval, Alain Boudet, Bruno Lanson, Jocelyne Ferret, Francois Marti

### ► To cite this version:

Eric Ferrage, Grégory Seine, Anne-Claire Gaillot, Sabine Petit, Philippe de Parseval, et al.. Structure of the 001 talc surface as seen by atomic force microscopy: Comparison with X-ray and electron diffraction results. *European Journal of Mineralogy*, 2006, 18, pp.483-491. 10.1127/0935-1221/2006/0018-0483 . hal-00192281

**HAL Id: hal-00192281**

**<https://hal.science/hal-00192281>**

Submitted on 27 Nov 2007

**HAL** is a multi-disciplinary open access archive for the deposit and dissemination of scientific research documents, whether they are published or not. The documents may come from teaching and research institutions in France or abroad, or from public or private research centers.

L'archive ouverte pluridisciplinaire **HAL**, est destinée au dépôt et à la diffusion de documents scientifiques de niveau recherche, publiés ou non, émanant des établissements d'enseignement et de recherche français ou étrangers, des laboratoires publics ou privés.



## 26 **Abstract**

27

28           In this study the surface structure of a centimetre sized crystal of talc from the  
29 Trimouns deposit (Ariège, France) was imaged by atomic force microscopy. The direct image  
30 shows detailed characteristics of clay tetrahedral surfaces. The unit-cell dimensions obtained  
31 using atomic force microscopy ( $a_{\text{or}} = 5.47 \pm 0.28$  and  $b_{\text{or}} = 9.48 \pm 0.28$  Å) are found to be  
32 slightly higher, with an increased uncertainty, than those obtained using X-ray diffraction  
33 ( $a_{\text{or}} = 5.288 \pm 0.007$  and  $b_{\text{or}} = 9.159 \pm 0.010$  Å) and selected-area electron diffraction  
34 ( $a_{\text{or}} = 5.32 \pm 0.03$  and  $b_{\text{or}} = 9.22 \pm 0.05$  Å). Talc has a quasi-ideal surface, clean of strong  
35 structural distortion as compared to most of other clay minerals and unlikely surface  
36 relaxation. The observation on the obtained image of apparent cell dimension enlargement is  
37 then more likely attributed to instrumental artefacts, also responsible for scattered values of  
38 unit-cell parameters rather than related to any surface structural features.

39

40 Key-words : talc, atomic-force microscopy, surface structure, X-ray diffraction, selected-area  
41 electron diffraction.

42

## 43 **1. Introduction**

44

45           Because of its beneficial properties to manufactured products, talc is widely used in  
46 paper coating, paint, ceramics, and polymer industries. In the automotive industry, talc is  
47 added to polymers to stabilize and harden automobile spare parts such as fenders, dashboards,  
48 steering wheels, etc. However, because different talc varieties can exhibit a wide range of  
49 physical and chemical properties it is necessary to optimize the use of these different types of  
50 talc for specific industrial applications. In particular, it is necessary to take into account the

51 surface structure of talc which, for example, may or may not allow the epitaxial growth of  
52 polymers (Ferrage *et al.*, 2002).

53 Over the last decade, the availability of atomic force microscopes (AFM) has provided  
54 new insights into mineral reactivity by providing images of crystal growth or dissolution at  
55 the micro-to-nanometer scale (Hillner *et al.*, 1992a and b; Kuwahara *et al.*, 1998, 2001;  
56 Bosbach *et al.*, 2000; Lindgren, 2000; Bickmore *et al.*, 2001; Brandt *et al.*, 2003; Tournassat  
57 *et al.*, 2003; Aldushin *et al.*, 2004; Yokoyama *et al.*, 2005). AFM has also allowed the direct  
58 visualization of the outer surfaces of minerals by imaging either groups of atoms at the  
59 molecular scale (Drake *et al.*, 1989; Weisenhorn *et al.*, 1990; Hartman *et al.*, 1990; Johnson *et*  
60 *al.*, 1991; Drake & Hellmann 1991; Wicks *et al.*, 1992, 1993, 1998; Vrdoljak *et al.*, 1994;  
61 Kuwahara, 1999, 2001) or individual atoms (Lindgreen *et al.*, 1991; Wicks *et al.*, 1992;  
62 Vrdoljak *et al.*, 1994; Sokolov *et al.*, 1997, 1999). Because of their perfect cleavage along the  
63 {001} plane, which produces extremely flat external surfaces, phyllosilicates are especially  
64 well-suited for an AFM study.

65 The structure of talc differs from that of mica, chlorite or lizardite which were  
66 previously imaged by AFM (Hartman *et al.*, 1990; Wicks *et al.*, 1992, 1993, 1998; Vrdoljak  
67 *et al.*, 1994; Kuwahara, 1999, 2001; Lindgreen *et al.*, 1991). Talc structure presents two  
68 similar external tetrahedral faces which is suitable for microscopic observations. In addition,  
69 the excess of octahedral charges is compensated for by deficiency in tetrahedral charges  
70 (Martin *et al.*, 1999), and the 2:1 sheet remains neutral, the interlayer of talc being thus devoid  
71 of cations. Finally, the weak substitution in talc layers induce moderate structural distortions  
72 such as tilts or tetrahedral rotations.

73 In this article we report the first atomic force microscope images of the surface of a  
74 talc sample composed of very well-stacked layers from the Trimouns deposit (Ariège,  
75 France). Images of the talc surface obtained from traditional AFM in repulsive mode are

76 compared with data in the literature and structural parameters of the bulk structure obtained  
77 from X-ray diffraction (XRD) and selected-area electron diffraction (SAED).

78

79

## 80 **2. Background**

81

### 82 *2.1. Geological setting and sampling*

83 Talc (2:1 layer silicate) has a composition close to that of the  $[\text{Mg}_3\text{Si}_4\text{O}_{10}(\text{OH})_2]$  end-  
84 member but with minor amounts of Fe, Al and F, and traces of Mn, Ti, Cr, Ni, Na and K  
85 (Heller-Kallai & Rozenson, 1981; Noack *et al.*, 1986; Abercrombie *et al.*, 1987; Aramu *et al.*,  
86 1989; Coey *et al.*, 1991; de Parseval *et al.*, 1991, 1993; Martin *et al.*, 1996, 1999). The sample  
87 comes from the Trimouns talc and chlorite deposit, located in the French Pyrenees, ~100 km  
88 south of Toulouse, at an altitude of 1,700 m. The origin of talc is well-established and is the  
89 result of the hydrothermal alteration of wallrock in a zone of intense shearing between the  
90 Saint Barthélémy dome and the low-grade Paleozoic metamorphic cover (Fortuné *et al.*, 1980;  
91 Moine *et al.*, 1982, 1989; de Parseval *et al.*, 1993). Dolostones of the Paleozoic cover were  
92 transformed to talc, whereas the more siliceous and aluminous rocks (micaschists and granitic  
93 pegmatites) evolved to a chlorite-dominant ore characterized by well-defined metasomatic  
94 zones. The sampled talc of centimetric flakes that is commonly referred to as "talc flower"  
95 when mined, was formed within geodes in the dolomite hanging wall of the ore body and is  
96 associated with REE-minerals (de Parseval *et al.*, 1997).

97

### 98 *2.2. Crystallographic data*

99 Talc is a 2:1 phyllosilicate structure (Fig. 1a) with two Si tetrahedral sheets (forming  
100 an array of hexagonal rings of  $\text{SiO}_4$  tetrahedra – Fig. 1b) each linked through the apical

101 oxygen to either, and leading to the presence in between of a sheet of octahedrally  
102 coordinated Mg<sup>2+</sup> cations. Early structural characterizations of talc have described its  
103 structure as monoclinic (*C-1* space group – Gruner, 1934), but later publications have  
104 described it as triclinic (*C-1* space group - Rayner & Brown, 1973) or as pseudomonoclinic  
105 (*Cc*) but using a *P-1* space group (Perdikatsis & Burzlaff, 1981). In comparison to aluminous  
106 phyllosilicates the misfit in lateral dimensions between tetrahedral and octahedral sheets is  
107 smaller, leading to a better accommodation of the two sheets. As a result, the tetrahedral  
108 rotation angle is diminished from ~13-14° for muscovite to ~3-4° for talc (Radoslovitch,  
109 1961, 1962). The tetrahedral tilt angle out of the basal oxygen plane is very weak, giving an  
110 essentially flat {001} surface. The moderate tetrahedral rotations induce a reduction of the  
111 SiO<sub>4</sub> ring symmetry from hexagonal into ditrigonal (Fig. 1b).

112

### 113 **3. Experimental Methods**

114

#### 115 *3.1. Chemical analyses*

116 The chemical composition of the talc sample used in this study was determined using a  
117 Cameca SX50 electron microprobe. The sample was included in a resin and polished to obtain  
118 perfect flat section. Operating conditions were 15 kV and 10 nA with beam size set to  
119 3×3 μm. Standards used for calibration were: wollastonite for Si, corundum for Al, periclase  
120 for Mg, haematite for Fe, pyrophanite for Mn and topaze for F.

121

#### 122 *3.2. X-ray diffraction*

123 To obtain information on the crystallographic parameters, particularly in the ab plane,  
124 XRD data was collected on a randomly oriented sample. The centimetric talc flakes were  
125 ground to a fine powder in an agate mortar. XRD data was collected with a Bruker D5000

126 diffractometer equipped with a Kevex Si(Li) solid-state detector and CuK $\alpha$  radiation.  
127 Intensities were recorded at a 0.02 $^{\circ}$ 2 $\theta$  interval, from 2 to 90 $^{\circ}$ , using a 50 sec counting time per  
128 step. Accuracy on 2 $\theta$  positions was better than 0.001 $^{\circ}$ . A rotating sample holder was used to  
129 minimize the effect of preferential orientation. The openings of the divergence slit, the two  
130 Soller slits, the antiscatter slit, and the resolution slit were 0.5 $^{\circ}$ , 2.3 $^{\circ}$ , 2.3 $^{\circ}$ , 0.5 $^{\circ}$  and 0.06 $^{\circ}$ ,  
131 respectively. Cell parameters were refined using U-Fit 1.3 software assuming a *P-1* space  
132 group (Perdikatsis & Burzlaff, 1981).

133

### 134 3.3. $^{57}\text{Fe}$ Mössbauer spectroscopy

135 A  $^{57}\text{Fe}$  Mössbauer absorption spectrum of the talc was collected over the range  $\pm 4$   
136 mm.s $^{-1}$  with a 512 channels analyzer. The Mössbauer spectrometer is composed of a compact  
137 detector  $\gamma$ -system for high-counting rates and of a conventional constant-acceleration  
138 Mössbauer device (WISSEL). A  $^{57}\text{Co}$  (in Rh) source with nominal activity of 50 mCi was  
139 used. Talc flakes were finely ground under acetone (to minimize possible oxidation of Fe) and  
140 the resulting powder was placed in a plexiglas sample holder. The spectrum was recorded  
141 using a Canberra multichannel analyzer at 80 $^{\circ}$ K to benefit from the second-order Doppler  
142 effect. The isomer shift was recorded with respect to  $\alpha$ -Fe metal. As recommended by  
143 Rancourt *et al.* (1992), the absorption thickness of the talc sample was calculated to minimize  
144 the width of the absorption lines using data from the phlogopite-annite series as phlogopite  
145 has a similar Fe-content to that of talc so as. The values are around 200 mg of mineral per  
146 cm $^2$ . Lorentzian lines shapes were assumed for decomposition, based on least-squares fitting  
147 procedures. The  $\chi^2$  and misfit values were used to estimate the goodness of fit.

148

### 149 3.4. Selected-area electron diffraction

150 The electron diffraction study was performed on a Philips 420 transmission electron  
151 microscope (TEM) equipped with a tungsten filament and operated at 120kV. Talc flakes  
152 were gently crushing in distilled water and dispersed onto a 3mm holey carbon-coated Cu-  
153 mesh TEM grid. Selected-area electron diffraction (SAED) patterns were recorded after  
154 orienting talc single crystals along the [001] zone axis using a double-tilt sample holder. The  
155 camera constant of the talc SAED patterns was calibrated using a gold reference sample with  
156 the crystals oriented along [100]. SAED patterns were recorded under the same parallel beam  
157 illumination conditions for both gold and talc samples. The error on the camera constant was  
158 estimated to be ~0.7%. Distances between diffraction spots were measured on the negatives  
159 using a precision measurement table.

160

### 161 *3.5. Atomic force microscopy*

162 The talc surface was investigated by atomic force microscopy (AFM) using a  
163 Nanoscope II AFM from Digital Instruments. The talc sample was scanned in air using the  
164 repulsive contact mode with constant deflection. The D-head piezoelectric scanner was  
165 calibrated using HOP graphite and mica. The pyramidal shaped Si<sub>3</sub>N<sub>4</sub> cantilevers from Digital  
166 Instrument with 200 μm wide legs and a spring constant of 0.12 N.m<sup>-1</sup> were used. The talc  
167 sample was cleaved along {001} plane surface prior to observation using adhesive tape.  
168 Observations were performed using a vibration isolated platform and the thermal drift was  
169 minimized by waiting for the AFM to equilibrate with ambient temperature. Contact forces,  
170 scan speeds and scan directions were adjusted to optimize the resolution.

171

## 172 **4. Results**

173

### 174 *4.1. Mössbauer spectroscopy*

175 Table 1 lists the iron site-occupancies of the talc spectrum fitting, taking into account  
176 the quadrupole splitting distributions (Rancourt, 1994). The spectrum of the talc sample  
177 obtained at 80°K (Fig. 2a) is similar to talc spectra reported by Martin *et al.* (1999). It shows a  
178 difference in intensity between the two absorption bands, and a significant shoulder on the  
179 side of the -0.5 mm.s<sup>-1</sup> peak. A good fit to the experimental data was obtained with four  
180 Lorentzian doublets (Fig. 2b – Table 1). The first two, both with a large quadrupole splitting,  
181 are due to Fe<sup>2+</sup> in octahedral sites. The third doublet with a small quadrupole splitting and a  
182 low isomer shift is located within the first absorption band and attributed to Fe<sup>3+</sup> in the  
183 tetrahedral site (Dyar & Burns, 1986; Rancourt *et al.*, 1992; Rancourt, 1993; Martin *et al.*,  
184 1999). The last doublet corresponds to Fe<sup>3+</sup> in octahedral sites (Blaauw *et al.*, 1980; Dyar &  
185 Burns, 1986; Rancourt *et al.*, 1992; Dyar, 1993; Rancourt, 1993; Martin *et al.*, 1999).  
186 According to this decomposition, Fe<sup>3+</sup> cations are thus present in both octahedral and  
187 tetrahedral sites. However, Fe<sup>2+</sup> is the dominant iron species (81%), thus indicating reducing  
188 conditions during the formation of talc.

189

#### 190 4.2. Chemical composition

191 The structural formula of the talc sample was calculated on the basis of eleven  
192 oxygens from the average of ten bulk analyses obtained by electron microprobe:  
193  $[\text{Mg}_{2.890}\text{Fe}^{2+}_{0.023}\text{Mn}^{2+}_{0.003}\text{Fe}^{3+}_{0.002}\text{Al}_{0.002}]_{\Sigma 2.917} [\text{Si}_{4.030}\text{Fe}^{3+}_{0.003}\text{Al}_{0.001}]_{\Sigma 4.034} \text{O}_{10} (\text{OH}_{1.975}\text{F}_{0.025})$   
194  $\mu$ The distribution of iron between <sup>[6]</sup>Fe<sup>2+</sup>, <sup>[4]</sup>Fe<sup>3+</sup> and <sup>[6]</sup>Fe<sup>3+</sup> was deduced from Mössbauer  
195 spectroscopy results. Aluminum was split into <sup>[4]</sup>Al and <sup>[6]</sup>Al to insure the neutralization of  
196 charges in the octahedral and the tetrahedral sheets, leading to the electroneutrality of the  
197 layer. The composition of the talc sample is thus very close to that of the representative talc  
198 determined by Martin *et al.* (1999) for the Trimouns deposit. Only minor substitutions are

199 present in the octahedral or tetrahedral sites leading to moderate local distortions in the  
200 tetrahedral sheet and thus to a nearly flat {001} surface.

201

#### 202 4.3. X-ray diffraction

203 The powder diffraction pattern of the ground talc powder is characteristic of pure talc  
204 with sharp 00 $\ell$  reflections that form a harmonic series ( $d_{001} = \ell \cdot d_{00\ell}$ ) thus indicating a well-  
205 ordered structure along the  $c^*$  axis without interstratification of chlorite layers (Fig. 3). Traces  
206 of quartz and dolomite are also detected. Sample unit-cell parameters were refined in the  
207 triclinic system ( $P-1$  space group - Perdikatsis & Burzlaff, 1981) from the positions of all  
208 measurable reflections between 2 and 90°2 $\theta$ . Unit-cell parameters from the present study are  
209 in agreement with those reported by Perdikatsis & Burzlaff (1981 – Table 2). It is possible to  
210 deduce the  $a_{or}$  and  $b_{or}$  dimensions of the usual C-centered pseudo-orthogonal unit cell from  
211 the refined abc unit-cell parameters defined in the triclinic system (Fig. 1b). As the  $\gamma$  angle is  
212 close to 120°,  $a_{or}$  is similar to  $a$  and  $b_{or}$  can be calculated as  $b_{or} = a_{or}\sqrt{3}$  (Table 2).

213

#### 214 4.4. Selected-area electron diffraction

215 The SAED pattern of a talc single crystal observed along the [001] zone axis contains  
216 very sharp  $hk0$  diffraction spots arranged according to a pseudo-hexagonal pattern (Figure 4).  
217 In order to determine unit-cell dimensions in the  $\mathbf{a}^*\mathbf{b}^*$  plane,  $a_1^*$ ,  $a_2^*$  and  $a_3^*$  distances were  
218 measured along [100], [010] and [110], respectively, and averaged to a single  $a^*$  dimension.  
219 Measurements were repeated for twelve crystals perfectly aligned along [001], and all values  
220 were then averaged to obtain a single  $a^*$  unit-cell dimension in the reciprocal space. However,  
221 in order to determine the unit-cell dimension in the  $\mathbf{ab}$  plane in the direct space, it is necessary  
222 to take into account the 3D symmetry of the unit-cell:

$$223 \quad a = (\sin \alpha / a^*) / [1 + 2 \cdot \cos \alpha \cdot \cos \beta \cdot \cos \gamma - \cos^2 \alpha - \cos^2 \beta - \cos^2 \gamma]^{-2} \quad (1)$$

224 As talc crystallizes in a triclinic system, unit-cell dimensions in the direct space cannot be  
225 simply deduced from the distances measured on the SAED pattern without making some  
226 assumptions for the values of  $\alpha$ ,  $\beta$  and  $\gamma$  angles. Therefore,  $\alpha$ ,  $\beta$  and  $\gamma$  values from XRD  
227 analysis (Table 2) were used in Eq. 1, and the following relationship was then obtained:

$$228 \quad a = 1.1545/a^* \quad (2)$$

229 Note that the same relationship can be obtained, without using results from XRD, if one  
230 assumes that (i) the  $\gamma$  angle is close to  $120^\circ$ , and that (ii) the  $\alpha$  and  $\beta$  angles are between 85  
231 and  $100^\circ$  then the approximations  $\sin\alpha \sim 1$  and  $\cos^2\alpha \sim \cos^2\beta \sim \cos\alpha \cdot \cos\beta \sim 0$  can be used. It  
232 follows that from direct measurements of the SAED patterns and from the relation given  
233 above (Eq. 2), it is possible to deduce that  $a_{\text{or}} = a = 5.32(3) \text{ \AA}$  and that  $b_{\text{or}} = a_{\text{or}} \sqrt{3} = 9.22(5) \text{ \AA}$   
234 (Table 2).

235

#### 236 *4.5. Atomic force microscopy*

237

##### 238 *Micro-topography of cleaved surface*

239 A high-resolution image was recorded to observe the talc surface micro-topography  
240 ( $500 \times 500 \text{ nm}^2$  – Fig. 5). Talc sample exhibits thick crystals in agreement with the  
241 macrocrystalline character of the investigated sample. A perpendicular section of talc  
242 topography is shown in Figure 5d and reveals that after cleavage these crystals are several  
243 tens of unit layers thick. This sample also has very large domains with flat surfaces which are  
244 particularly suitable for AFM imaging. Note the variation in Z direction on these almost flat  
245 regions that can be attributed to cantilever vibration which is greater when recording in air  
246 condition as contrast to images recorded in liquid (Kuwahara *et al.*, 1998, 2001). These  
247 regions were chosen for recording molecular-scale image.

248

249 *Molecular scale*

250 The raw image obtained at the molecular scale ( $5 \times 5 \text{ nm}^2$  - Fig. 6) shows an alignment  
251 of triangles on the tetrahedral sheet surface. The of this raw image allows determining the  $m_i$   
252 periodicity between adjacent triangles and the  $n_i$  periodicities for the second neighbor  
253 triangles along the perpendicular direction. Figure 7a shows the two-dimensional (2D) fast  
254 Fourier transform (FFT) of the raw image. On this numerical diffraction pattern, spots are  
255 distributed according to a pseudo-hexagonal pattern and different orders are visible that  
256 indicate a well-defined periodic surface structure. It is then possible to index these spots  
257 which correspond to  $m_i$  and  $n_i$  periodicities along two perpendicular directions in the raw  
258 image (Fig. 7b). The regularity of the structure deduced from the sharpness of the diffraction  
259 spots on 2D FFT is confirmed by direct periodicity measurements done on the raw image and  
260 reported in Figure 8, and leading to mean values of  $5.47 \pm 0.28 \text{ \AA}$  and  $9.48 \pm 0.28 \text{ \AA}$  for  $m_i$  and  
261  $n_i$  periodic distances, respectively.

262

## 263 **5. Discussion**

264

### 265 *5.1 Surface structure of talc*

266 The raw image of talc surface (Fig. 6) is consistent with those found in the wealth of  
267 literature devoted to AFM studies of tetrahedral sheet surfaces of phyllosilicates. If some  
268 images present an arrangement of hexagonal rings corresponding to the basal oxygen plane of  
269 tetrahedral sheet other images, obtained on micas, show a bright spot periodicity of about  
270  $5.1 - 5.3 \text{ \AA}$  (which could correspond to the layer unit-cell parameter of most phyllosilicates –  
271 Hartman et al., 1990; Lindgreen *et al.*, 1991; Wicks *et al.*, 1992, 1993; Vrdoljak *et al.*, 1994;  
272 Kuwahara, 1999, 2001). This periodicity was initially interpreted as the hexagonal array of  
273 interlayer cations but Kuwahara (1999) showed that it was possible to obtain both types of

274 image by varying the scan angle on the same sample. In addition, basal oxygen surface often  
275 show the alternation of high and low positions for any tetrahedron defining a hexagonal ring.  
276 This feature was first interpreted as resulting from the tetrahedral tilt of the basal oxygens but  
277 is now commonly considered as a topography artefact induced by the interaction between an  
278 asymmetric, double-atom, cantilever tip and the surface atoms (Gould *et al.*, 1989; Vrdoljak  
279 *et al.*, 1994; Wicks *et al.*, 1998; Kuwahara, 1999, 2001). According to these studies, triangles  
280 on the unfiltered image (Fig. 6) represent a height exaggerated of half of a tetrahedra. Thus,  
281 m- and n- periodicities between adjacent triangles correspond to  $a_{or}$  and  $b_{or}$  unit-cell  
282 dimensions of talc. Although the AFM image was recorded in air, the image is most likely of  
283 the basal oxygen surface rather than of some adsorbed species on the talc surface. Such  
284 adsorption would indeed result in a blurry image with holes and/or aggregation of these  
285 molecules. However, because cantilever drift easily removes interlayer cations from the mica  
286 surface, in spite of the strong electrostatic binding forces (Kuwahara, 1999, 2001), a similar  
287 “cleaning” of adsorbed species from the uncharged talc surface is most likely to occur.

288         The 2D FFT in which pseudo-hexagonal pattern was shown with different orders has  
289 indicated a well-defined periodic structure (Fig. 7). Back 2D FFT is commonly applied to  
290 remove extraneous signal from images but appears to be a controversial method. The two  
291 main criticisms are: i) important features of the raw image are removed and/or features that  
292 were not initially present are introduced, and ii) atomic positions are averaged. Wicks *et al.*  
293 (1998) discussed thoroughly these potential pitfalls, pointing out that the first point is  
294 essentially dependent on the competence of the user who should check carefully the FFT  
295 spots. Then, if all the structure information is used in the back 2D FFT operation, only high-  
296 frequency noise is removed, and the overall image enhancement does not affect structure  
297 details. Wicks *et al.* (1998) also demonstrated that following this image processing, atoms  
298 displaced from their ideal positions were not averaged as initially supposed. Figure 9a shows

299 the filtered image from the back 2D FFT of areas outlined on the numerical diffraction pattern  
300 (Fig. 7a). The filtered image (Fig. 9a) is essentially similar to the raw image (Fig. 6) but  
301 shows a spectacular enhancement of structural features, mainly alternate tetrahedra. The  
302 individual tetrahedra positions can be drawn to reveal the surface structure of talc (Fig. 9b).  
303 Note the presence of a small “hump” in the siloxane cavity. However, because of evident  
304 artefacts due in particular to the interaction between the double-atom cantilever tip and the  
305 sample, extreme care should be taken in the interpretation of these features in structural terms.

306

### 307 *5.2 Talc unit-cell parameters*

308 To determine the unit-cell dimension of the talc surface layer, approximately 100  
309 measurements in each of the m and n three directions (corresponding to  $\mathbf{a}_{\text{or}}$  and  $\mathbf{b}_{\text{or}}$  directions,  
310 respectively) were performed on the raw images (Fig. 8). The frequency distribution of m and  
311 n indicates a single-mode distribution for each which agrees with published distributions  
312 (Vrdoljak *et al.*, 1994; Kuwahara, 1999, 2001).

313 The  $a_{\text{or}}$  and  $b_{\text{or}}$  parameters measured on the talc surface by AFM are  $5.47 \pm 0.28 \text{ \AA}$  and  
314  $9.48 \pm 0.28 \text{ \AA}$ , respectively (Table 2). The uncertainty is quite high ( $\sim 5\%$  and  $3\%$  for  $a_{\text{or}}$  and  
315  $b_{\text{or}}$ , respectively), but is consistent with other AFM studies on clay minerals (between  $\sim 2\%$   
316 and  $8\%$ , *e.g.*, Vrdoljak *et al.*, 1994; Kuwahara, 1999, 2001) regardless of the number of  
317 measurements performed on a single image and of the number of images processed. The  
318 obtained range for  $a_{\text{or}}$  and  $b_{\text{or}}$  parameters includes the values expected from the bulk structure  
319 determination although the mean values are high. Similar large unit cell parameters have been  
320 reported for other phyllosilicates, but the uncertainty systematically includes the ideal unit-  
321 cell dimensions (Vrdoljak *et al.* (1994) and Kuwahara (1999) on chlorite and muscovite,  
322 respectively). This enlargement of unit-cell parameters was attributed to surface relaxation.  
323 However, in contrast to micas or chlorite, no interlayer sheet or cation contributes to

324 interlayer cohesion in talc. As a result, surface relaxation is unlikely for talc and the observed  
325 variation in unit-cell dimensions may rather be attributed to instrumental effects as evoked by  
326 Vrdoljak *et al.* (1994). Note that improved unit-cell dimensions could be obtained by  
327 recording images in liquid environment rather than in air conditions as done in the present  
328 study (Kuwahara 1999, 2001; Sokolov *et al.*, 1997, 1999;).

329         Unit-cell dimensions obtained from XRD and SAED are consistent (Table 2) despite  
330 difficulties intrinsic to SAED such as the calibration of the camera constant, the alignment of  
331 a single crystal along [001] and the inability to precisely determine  $\alpha$ ,  $\beta$  and  $\gamma$  angles for a  
332 triclinic system. Moreover, the uncertainty on the measured values is low for the two methods  
333 ( $\sim 0.1\%$  and  $0.6\%$  for XRD and SAED, respectively – Table 2). In contrast,  $a_{or}$  and  $b_{or}$   
334 parameters measured on the talc surface by AFM are scattered and the resulting uncertainty  
335 on the unit-cell parameter is much higher as discussed above. XRD and SAED (providing a  
336 good calibration of the camera constant) are more accurate methods to determine unit-cell  
337 parameters because of the improved statistics (for XRD) and of the enhanced sensitivity to  
338 crystal geometry.

339         Because the sample used in the present study presents a quasi-ideal surface structure  
340 with extremely limited tetrahedral tilts/rotations and limited, if any, surface relaxation, the  
341 variation in unit-cell dimensions can therefore rather be attributed to instrumental variability  
342 (calibration, tip-sample interaction). Extreme care should thus be used when interpreting the  
343 changes in unit-cell dimensions in terms of structural features for other clay minerals such as  
344 micas, kaolinites and chlorites in which such structural deformations are likely

345

## 346 **6. Conclusion**

347

348 In relation with the peculiar crystallinity of the studied talc sample from the Trimouns  
349 deposit (Ariège, France), it has been possible using atomic force microscopy to obtain a  
350 detailed image of the talc surface at the molecular scale. However, in spite of the high-quality  
351 image obtained, artefacts that lead to the observation of only one tetrahedron out of two were  
352 detected (double-atom cantilever tip interaction). In addition, the very peculiar crystal-  
353 chemistry of talc (very limited tetrahedral tilts and tetrahedral rotations, unlikely structure  
354 relaxation) has revealed the existence of additional instrumental effects. These effects lead to  
355 a slight distortion of the image that make a structural interpretation of these distortions,  
356 described in previous studies for other clay minerals (micas, chlorites), ambiguous. Finally  
357 the comparison of structure dimensions with data obtained by XRD and SAED shows AFM  
358 limitations for unit-cell dimensions determination because of the increased uncertainty and of  
359 the possible distortion (enlargement) by instrumental effects.

360

### 361 *Acknowledgements*

362

363 EF and FM are grateful to the S.A. Talc de Luzenac for financial support. TEM  
364 analyses were supported by NSF grant #EAR0409071. Fruitful discussions with Dirk  
365 Bosbach (INE – Karlsruhe, Germany) and instructive comments on an earlier version of the  
366 manuscript by Alain Baronnet (CRMCN Marseille, France) are also greatly acknowledged.  
367 This study has benefited of technical assistance from the Laboratoire de Chimie de  
368 Coordination (Toulouse, France) for Mössbauer analysis. The manuscript was much improved  
369 by the constructive reviews of Fred Wicks, Yoshihiro Kuwahara and AE Kenneth Livi.

## References

- 370  
371
- 372 Abercrombie, H.J., Skippen, G.B. and Marshall, D.D. (1987): F-OH substitution in natural  
373 tremolite, talc, and phlogopite. *Contrib. Mineral. Petr.*, **97**, 305-312.
- 374 Aldushin, K., Jordan, G., Fechtelkord, M., Schmahl, W.W., Becker, H.W., Rammensee, W.  
375 (2004): On the mechanisms of apophyllite alteration in aqueous solutions. A combined  
376 AFM, XPS and MAS NMR study. *Clay. Clay Miner.*, **52**, 432-442.
- 377 Aramu, F., Maxiav, G., Delunas, A. (1989): Mössbauer spectroscopy of talc minerals. *Nuovo*  
378 *Cimento*, **11D**, 891-896.
- 379 Bickmore, B.R., Bosbach, D., Hochella, M.F., Charlet, L., Rufe E. (2001): In situ atomic  
380 force microscopy study of hectorite and nontronite dissolution: Implications for  
381 phyllosilicate edge surface structures and dissolution mechanisms. *Am. Mineral.*, **86**,  
382 411-423.
- 383 Blaauw, C., Stroink, G., Leiper, W. (1980): Mössbauer analysis of talc and chlorite. *J. Phys. I*,  
384 **41**, 411-412.
- 385 Bosbach, D., Charlet, L., Bickmore, B.R., Hochella, M.F.J. (2000): The dissolution of  
386 hectorite: In-situ, real-time observations using Atomic Force Microscopy. *Am.*  
387 *Mineral.*, **85**, 1209-1216.
- 388 Brandt, F., Bosbach, D., Krawczyk-Barsch, E., Arnold, T., Bernhard, G. (2003): Chlorite  
389 dissolution in the acid pH-range: A combined microscopic and macroscopic approach.  
390 *Geochim. Cosmochim. Ac.*, **67**, 1451-1461.
- 391 Coey, J.M.D., Bakas, T., Guggenheim, S. (1991): Mössbauer spectra of minnesotaite and  
392 ferrous talc. *Am. Mineral.*, **76**, 1905-1909.
- 393 De Parseval, P., Fontan, F., Aigouy, T. (1997): Composition chimique des minéraux de terres  
394 rares de Trimouns (Ariège, France). *C.R. Acad. Sci. II*, **234**, 625-630.

- 395 De Parseval, P., Fournes, L., Fortuné, J.P., Moine, B., Ferret, J. (1991): Distribution du fer  
396 dans les chlorites par spectrométrie Mössbauer (57Fe) : Fe(III) dans les chlorites du  
397 gisement de talc-chlorite de Trimouns (Pyrénées, France). *C.R. Acad. Sci. II*, **312**,  
398 1321-1326.
- 399 De Parseval, P., Moine, B., Fortuné, J.P., Ferret, J. (1993): Fluid-mineral interactions at the  
400 origin of the Trimouns talc and chlorite deposit (Pyrénées, France). in “Current  
401 Research in Geology Applied to Ore Deposits”, P. Fenoll Hach-Ali, J. Torres-Ruiz, F.  
402 Gervilla, eds. Univ. of Granada, Granada, 205-209.
- 403 Drake, B., Prater, C.B., Weisenhorn, A.L., Gould, S.A.C., Albrecht, T.R., Quate, C.F.,  
404 Cannell, D.S., Hansma, H.G., and Hansma, P.K. (1989): Imaging crystals, polymers,  
405 and process in water with atomic force microscope. *Science*, **243**, 1586-1589.
- 406 Drake, B. & Hellmann, R. (1991): Atomic force microscopy imaging of the albite (010)  
407 surface. *Am. Mineral.*, **76**, 1773-1776.
- 408 Dyar, M.D. (1993): Mössbauer spectroscopy of tetrahedral Fe(III) in trioctahedral micas.  
409 Discussion. *Am. Mineral.*, **78**, 665-668.
- 410 Dyar, M.D. & Burns, R.G. (1986): Mössbauer spectral study of ferruginous one-layer  
411 trioctahedral micas. *Am. Mineral.*, **71**, 955-965.
- 412 Ferrage, E., Martin, F., Boudet, A., Petit, S., Fourty, G., Jouffret, F., Micoud, P., De Parseval,  
413 P., Salvi, S., Saint-Gérard, Y., Buratto, S., Ferret, J., Fortuné, J.P. (2002): Talc as  
414 nucleating agent of polypropylene : morphology induced by lamellar particles addition  
415 and interface mineral-matrix modelisation. *J. Mater. Sci.*, **37**, 1561-1573.
- 416 Fortuné, J.P., Gavaille, B., Thiebaut, J. (1980): Le gisement de talc de Trimouns près de  
417 Luzenac (Ariège). *Int. Geol. Congr.*, **26**, E10, 43 p.

418 Gould, S.A.C., Burke, K., Hansma, P.K. (1989): Simple theory for the atomic force  
419 microscope with a comparison of theoretical and experimental images of graphite.  
420 *Phys. Rev. B*, **40**, 5363-5366.

421 Gruner, J.W. (1934): The crystal structure of talc and pyrophyllite. *Z. Kristallogr. Krist.*, **88**,  
422 412-419.

423 Hartman, H., Sposito, G., Yang, A., Manne, S., Gould, S.A.C., Hansma, P.K. (1990):  
424 Molecular scale imaging of clay mineral surfaces with the atomic force microscope.  
425 *Clay. Clay Miner.*, **38**, 337-342.

426 Heller-Kallai, L. & Rozenson, I. (1981): The use of Mössbauer spectroscopy of iron in clay  
427 mineralogy. *Phys. Chem. Minerals*, **7**, 223-238.

428 Hillner, P.E., Gratz, A.J., Hansma, P.K. (1992a): Composite spiral growth kinetics of calcite  
429 revealed by AFM. *P. Soc. Photo-Opt. Inst.*, **1639**, 160-170.

430 Hillner, P.E., Manne, S., Hansma, P.K. (1992b): Atomic-scale imaging of calcite growth and  
431 dissolution in real time. *Geology*, **20**, 359-362.

432 Johnsson, P.A., Eggleston, C.M., Hotchella, M.F. Jr. (1991): Imaging molecular-scale  
433 structure and microtopography of hematite with the atomic force microscope. *Am.*  
434 *Mineral.*, **76**, 1442-1445.

435 Kuwahara, Y. (1999): Muscovite surface structure imaged by fluid contact mode AFM. *Phys.*  
436 *Chem. Minerals*, **26**, 198-205.

437 Kuwahara, Y. (2001): Comparison of the surface structure of tetrahedral sheets of muscovite  
438 and phlogopite by AFM. *Phys. Chem. Minerals*, **28**, 1-8.

439 Kuwahara, Y. Uehara, S., Aoki, Y. (1998) Surface microtopography of lath-shaped  
440 hydrothermal illite by tapping-mode and contact-mode AFM. *Clay. Clay Miner.*, **46**,  
441 574-582.

442 Kuwahara, Y. Uehara, S., Aoki, Y. (2001) Atomic force microscopy study of hydrothermal  
443 illite in Izumiyama pottery stone from Arita, Saga Prefecture, Japan. *Clay. Clay*  
444 *Miner.*, **49**, 300-309.

445 Lindgreen, H. (2000): Electrical conduction in layer silicates investigated by combined  
446 scanning tunnelling microscopy and atomic force microscopy. *Clay Miner.*, **35**, 643-  
447 652.

448 Lindgreen, H., Garnæs, J., Hansen, P.L., Besenbacher, F., Lægsgaard, E., Stensgaard, I.,  
449 Gould, S.A., Hansma, P.K. (1991): Ultrafine particles of North Sea illite/smectite clay  
450 minerals investigated by STM and AFM. *Am. Mineral.*, **76**, 1218-1222.

451 Martin, F., Ildefonse, P., Hazemann, J.L., Grauby, O., Decarreau, A. (1996): Random  
452 distribution of Ge and Si in synthetic talc: an EXAFS and FTIR study. *Eur. J.*  
453 *Mineral.*, **8**, 289-299.

454 Martin, F., Micoud, P., Delmotte, L., Marechal, C., Le Dred, R., De Parseval, P., Mari, A.,  
455 Fortuné, J.P., Salvi, S., Beziat, D., Grauby, O., Ferret, J. (1999): The structural  
456 formula of talc from the Trimouns deposit, Pyrénées, France. *Can. Mineral.*, **37**, 975-  
457 984.

458 Moine, B., Fortuné, J.P., Moreau, P., Viguiier, F. (1989): Comparative mineralogy,  
459 geochemistry and conditions of formation of two metasomatic talc and chlorite  
460 deposits : Trimouns (Pyrénées, France) and Rabenwald (Eastern Alps, Austria). *Econ.*  
461 *Geol.*, **84**, 1398-1416.

462 Moine, B., Gavoille, B., Thiebault, J. (1982): Géochimie des transformations à l'origine du  
463 gisement de talc et chlorite de Trimouns (Luzenac, Ariège, France). I - Mobilité des  
464 éléments et zonalités. *Bull. Mineral.*, **105**, 62-75.

465 Noack, Y., Decarreau, A., Manceau, A. (1986): Spectroscopic and oxygen isotopic evidence  
466 for low and high temperature origin of talc. *Bull. Mineral.*, **109**, 253-263.

467 Perdikatsis, B. & Burzlaff, H. (1981): Strukturverfeinerung am Talk  $Mg_3Si_4O_{10}(OH)_2$ . Z.  
468 *Kristallogr.*, **156**, 177-186.

469 Radoslovitch, E.W. (1961): Surface symmetry and cell dimensions of layer lattice silicates.  
470 *Nature*, **191**, 67-68.

471 Radoslovitch, E.W. (1962): The cell dimensions and symmetry of layer lattice silicates. I.  
472 Some structural considerations. II. Regression relations. *Am. Mineral.*, **47**, 599-636.

473 Rancourt, D.G. (1993): Mössbauer spectroscopy of tetrahedral Fe(III) in trioctahedral micas.  
474 Reply. *Am. Mineral.*, **78**, 669-671.

475 Rancourt, D.G. (1994): I. Inadequacy of lorentzian-line doublets in fitting spectra arising  
476 from quadrupole splitting distributions. *Am. Mineral.*, **21**, 244-249.

477 Rancourt, D.G., Dang, M.Z., Lalonde, A.E. (1992): Mössbauer spectroscopy of tetrahedral  
478 Fe(III) in trioctahedral micas. *Am. Mineral.*, **77**, 34-43.

479 Rayner, J.H. & Brown, G. (1973): The crystal structure of talc. *Clay. Clay Miner.*, **21**, 103-  
480 114.

481 Sokolov, I.Y., Henderson, G.S., Wicks, F.J. (1999): Theoretical and experimental evidence of  
482 "true" atomic resolution under non-vacuum conditions. *J. Appl. Phys.*, **86**, 5537-  
483 5540.

484 Sokolov, I.Y., Henderson, G.S., Wicks, F.J., Ozin, G.A. (1997): Improved atomic force  
485 microscopy resolution using an electric double layer. *Appl. Phys. Lett.*, **70**, 844-846.

486 Tournassat, C., Neaman, A., Villiéras, F., Bosbach, D., Charlet L. (2003): Nanomorphology  
487 of montmorillonite particles: Estimation of the clay edge sorption site density by low-  
488 pressure gas adsorption and AFM observations. *Am. Mineral.*, **88**, 1989-1995.

489 Vrdoljak, G.A., Henderson, G.S., Fawcett, J.J., Wicks, F.J. (1994): Structural relaxation of the  
490 chlorite surface imaged by the atomic force microscope. *Am. Mineral.*, **79**, 107-112.

491 Weisenhorn, A.L., Mac Dougell, J.E., Gould, Cox, S.A.C., Cox, S.D., Wise, W.S., Massie, J.,  
492 Maivald, P., Elings, V.B., Stucky, G.D., Hansma, P.K. (1990): Imaging and  
493 Manipulating Molecules on a Zeolite Surface with an Atomic Force Microscope.  
494 *Science*, **247**, 1330-1333.

495 Wicks, F.J., Henderson, G.S., Hawthorne, F.C., Kjoller, K. (1998): Evidence for atomic-scale  
496 resolution in atomic force microscopy of layer silicates. *Can. Mineral.*, **36**, 1607-1614.

497 Wicks, F.J., Kjoller, K., Eby, R.K., Hawthorne, F.C., Henderson, G.S., Vrdoljak, G.A. (1993)  
498 Imaging the internal atomic structure of layer silicates using the atomic force  
499 microscope. *Can. Mineral.*, **31**, 541-550.

500 Wicks, F.J., Kjoller, K., Henderson, G.S. (1992): Imaging the hydroxyl surface of lizardite at  
501 atomic resolution with the atomic force microscope. *Can. Mineral.*, **30**, 83-91.

502 Yokoyama, S., Kuroda, M., Sato, T., (2005): Atomic force microscopy study of  
503 montmorillonite dissolution under highly alkaline conditions. *Clay. Clay Miner.*, **53**,  
504 147-154.

505

**Tables**

506

507 **Table 1.** Mössbauer parameters of talc sample at 80 K. Quadrupole splitting ( $\Delta$ ) and isomer508 shift ( $\delta$ ) are given in  $\text{mm.s}^{-1}$ .

$\text{Fe}^{2+}$				$\text{Fe}^{3+}$				$\text{Fe}^{2+}$
$\delta^*$	$\Delta$	%	Site	$\delta^*$	$\Delta$	%	Site	$(\text{Fe}^{2+}+\text{Fe}^{3+})$
1.15	2.85			-0.25	0.21	12	[4]	
		81	[6]					81
1.21	2.96			0.07	0.68	7	[6]	

*Note:*  $\delta$  values relative to Fe-metal.

509

510 **Table 2.** Comparison of cell parameters. Distances are given in Angstroms and angles in511 degrees.  $a_{\text{or}}$  and  $b_{\text{or}}$  represent dimensions of the equivalent C-centered unit-cell with  $\gamma_{\text{or}} =$ 512  $90^\circ$ ).

	$a$	$b$	$c$	$\alpha$	$\beta$	$\gamma$	$a_{\text{or}}$	$b_{\text{or}}$
Perdikatsis & Burzlaff (1981)	5.291(3)	5.290(3)	9.460(5)	98.68(5)	85.27(5)	119.90(5)	5.293(4)	9.168(8)
XRD refinement (this study)	5.294(1)	5.281(1)	9.469(1)	98.71(1)	85.11(1)	119.98(1)	5.288(7)	9.159(10)
Electron diffraction (this study)	5.32(3)	-	-	-	-	-	5.32(3)	9.22(5)
AFM (this study)	-	-	-	-	-	-	5.47(28)	9.48(28)

*Note:* Unit-cell parameters from Perdikatsis & Burzlaff (1981) are transformed to appear in the  $C-I$  space group.

513

514

## Figure Captions

515  
516  
517  
518  
519  
520  
521  
522  
523  
524  
525  
526  
527  
528  
529  
530  
531  
532  
533  
534  
535  
536  
537  
538  
539  
540  
541

**Figure 1.** Talc structure along  $c^*$  (a) and the tetrahedral surface plane where a and b cell parameters in a quasi-orthogonal system ( $a_{or}$ ,  $b_{or}$ ) are indicated (b).

**Figure 2.** Experimental and fitted Mössbauer spectrum of talc sample at 80 K (a) and different components of the fitted spectrum (b).

**Figure 3.** X-ray-diffraction pattern of talc sample. Dol. and Qtz. represent dolomite and quartz traces, respectively.

**Figure 4.** SAED pattern of talc sample recorded along the [001] zone axis.

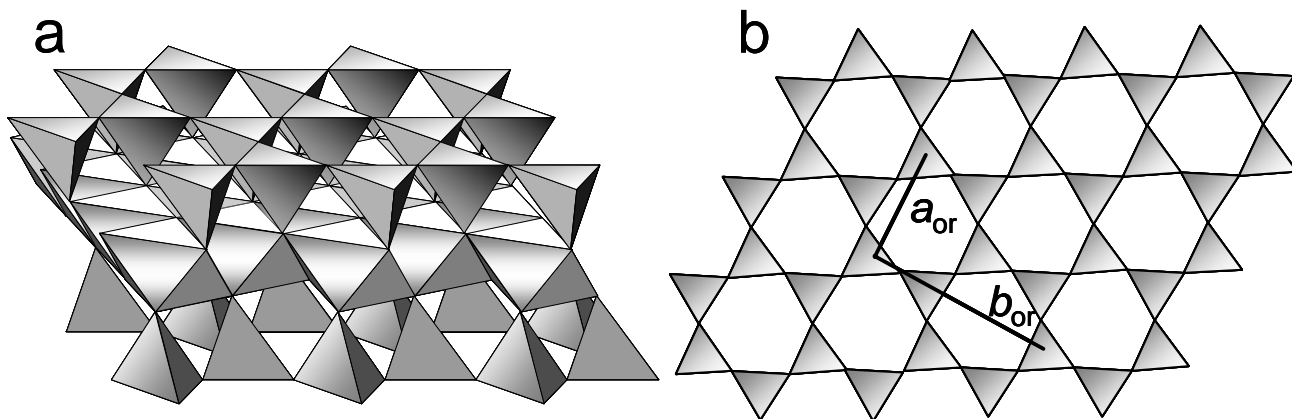
**Figure 5.** Micro-topography of talc surface (a) and the same image with isoaltitude curves separated by 70 Å to enhance topography contrasts (b). (c) and (d) represent profiles of cleaved surface morphology.

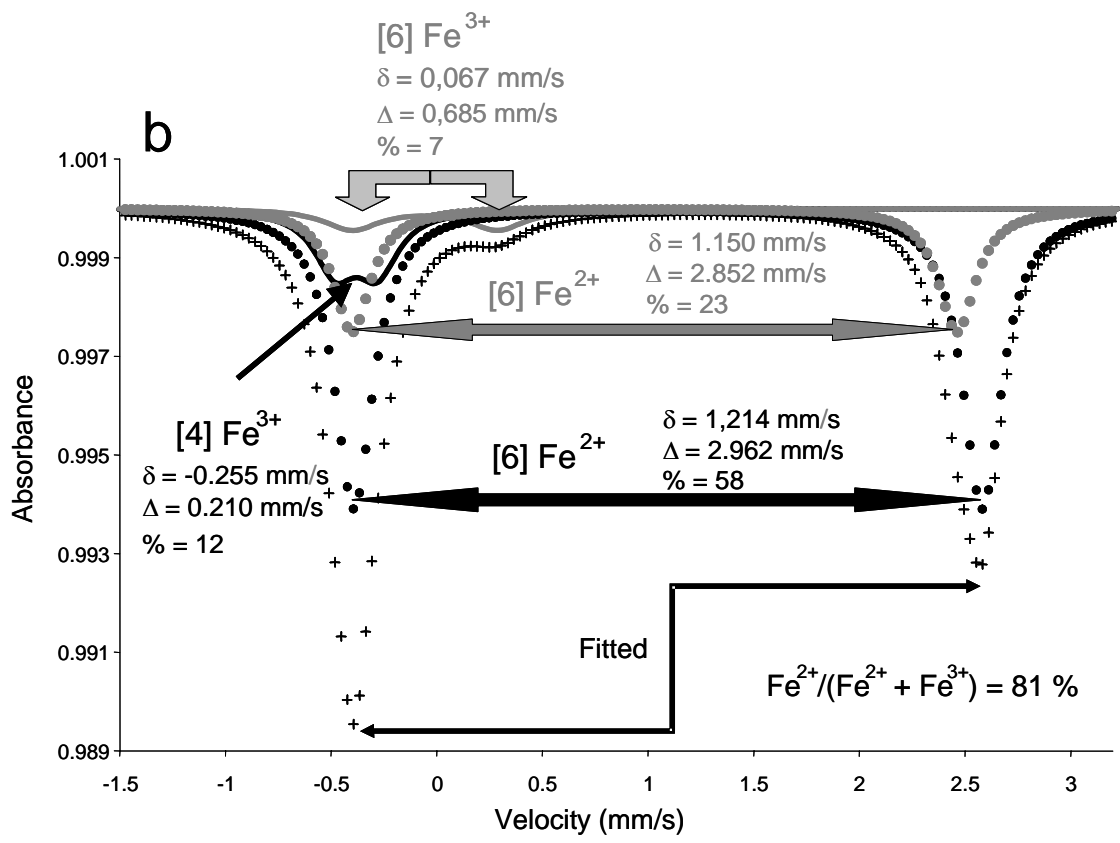
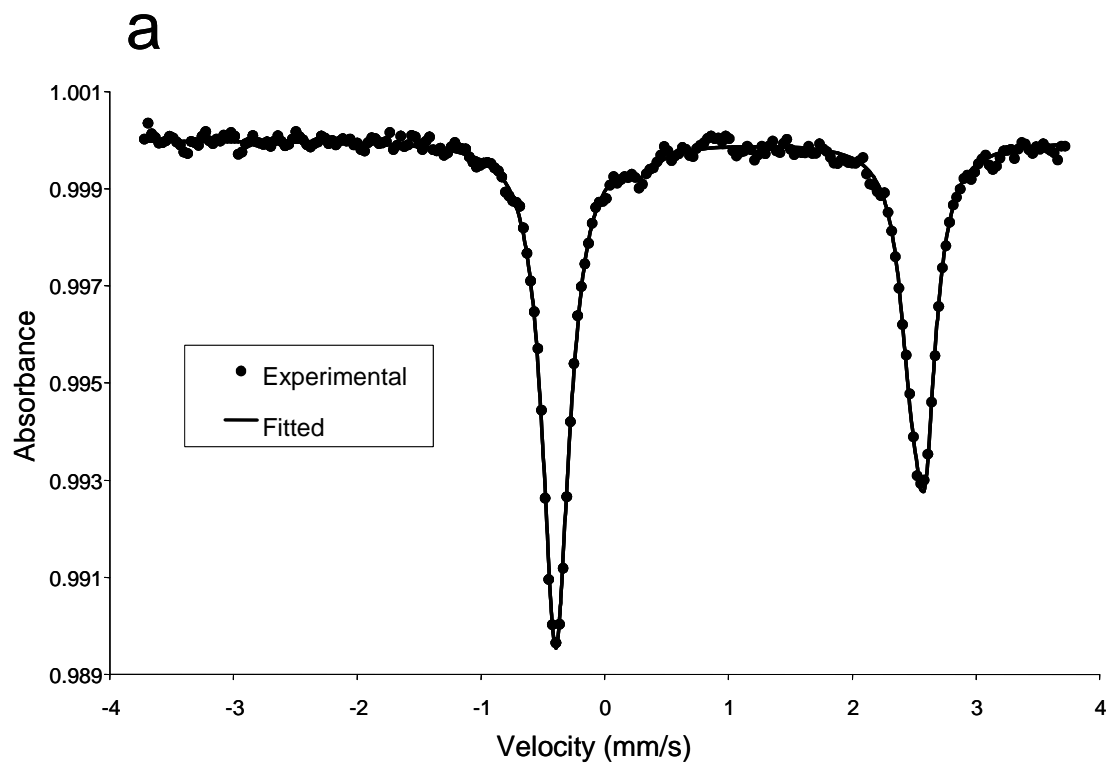
**Figure 6.** AFM image of talc surface at molecular scale  $5 \times 5 \text{ nm}^2$ .

**Figure 7.** Two-Dimensional Fourier Transform applied to molecular scale AFM image (Fig. 6 - a) and indexation of spots in reciprocal space (b).

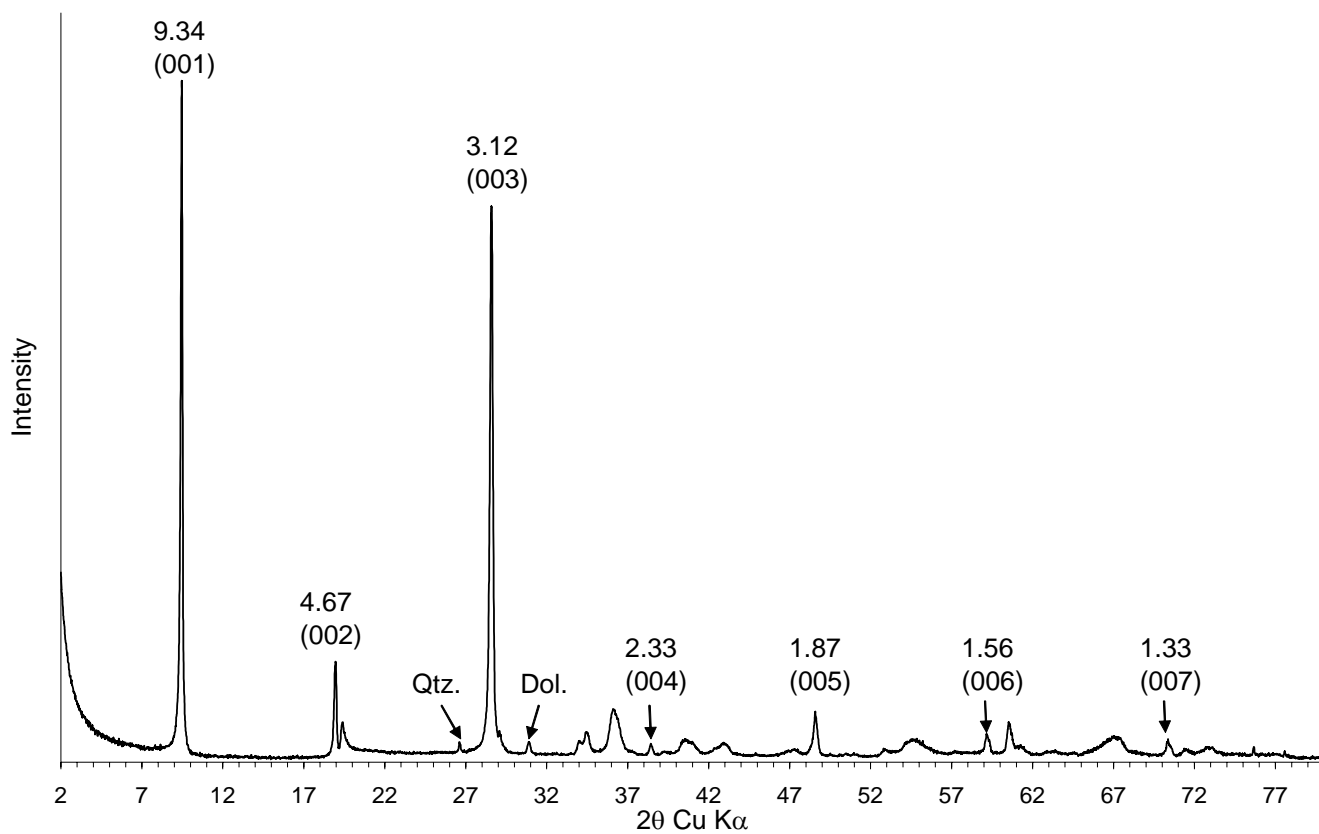
**Figure 8.** Histogram of  $a_{or}$  and  $b_{or}$  cell parameters from AFM molecular scale image.

**Figure 9.** Image shown in Fig. 5 after application of back 2D FFT to remove extraneous signal (a). An enlarged view of a image with a redraw of individual tetrahedrons (theoretical tetrahedral rotation not being taken into account).

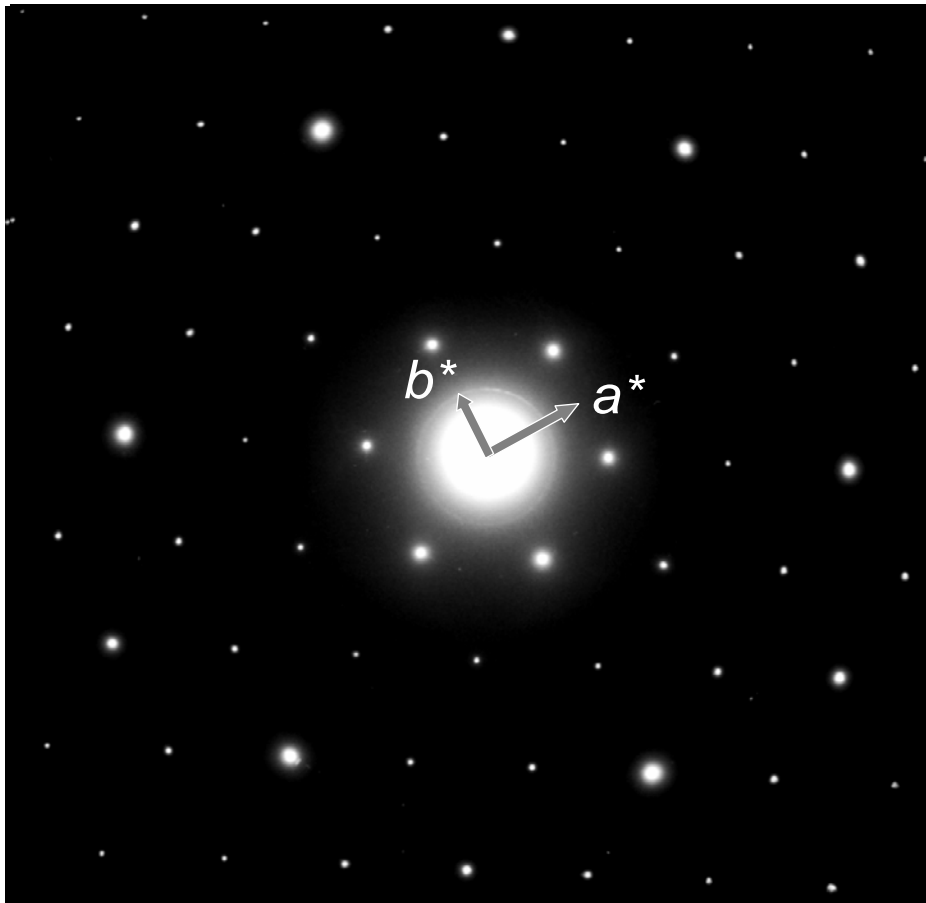




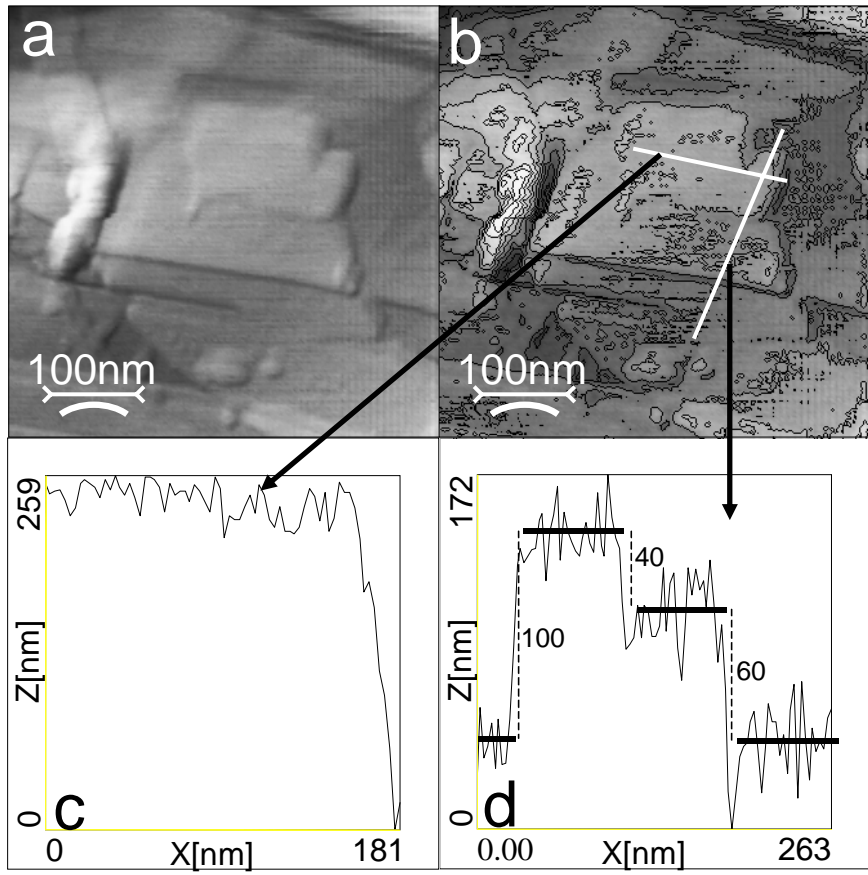
Ferrage et al., Fig. 02



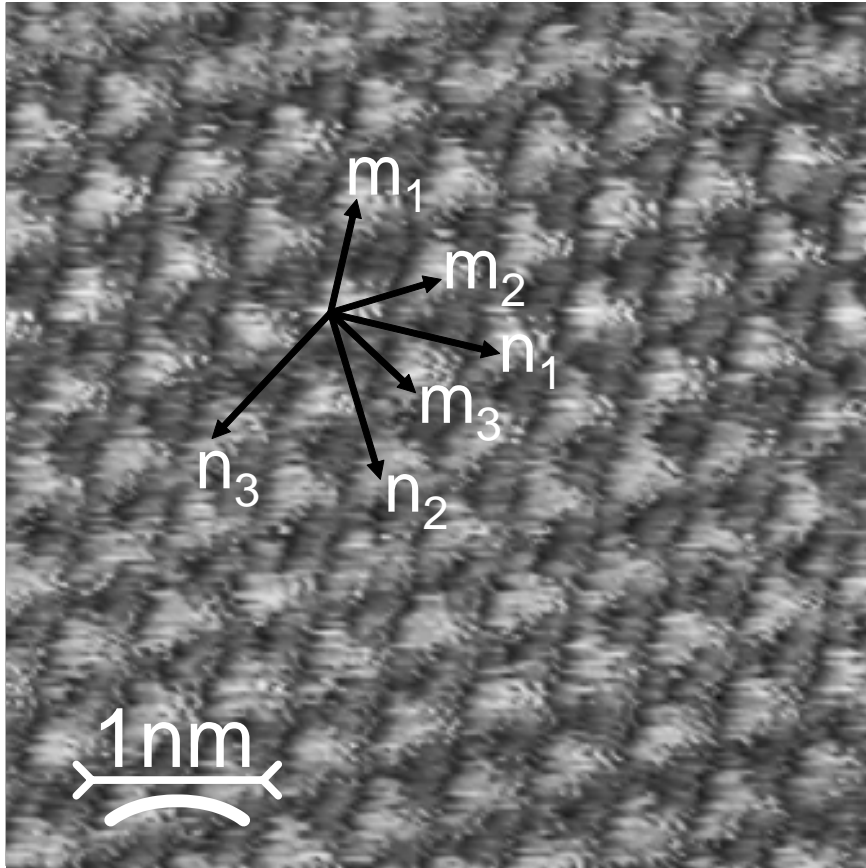
Ferrage et al., Fig. 03



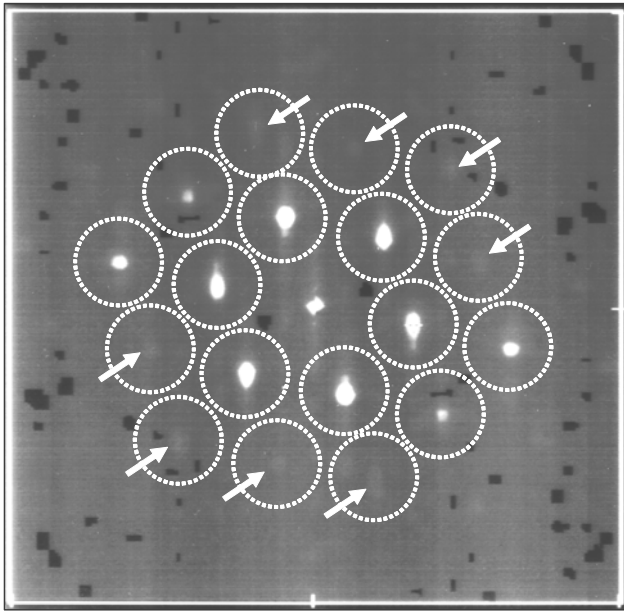
Ferrage et al., Fig. 04



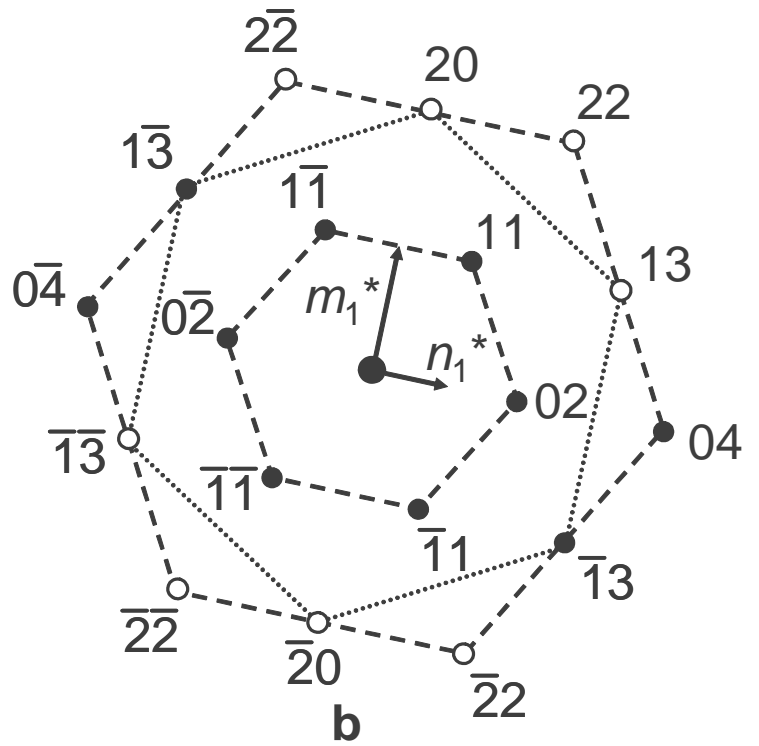
Ferrage et al., Fig. 05



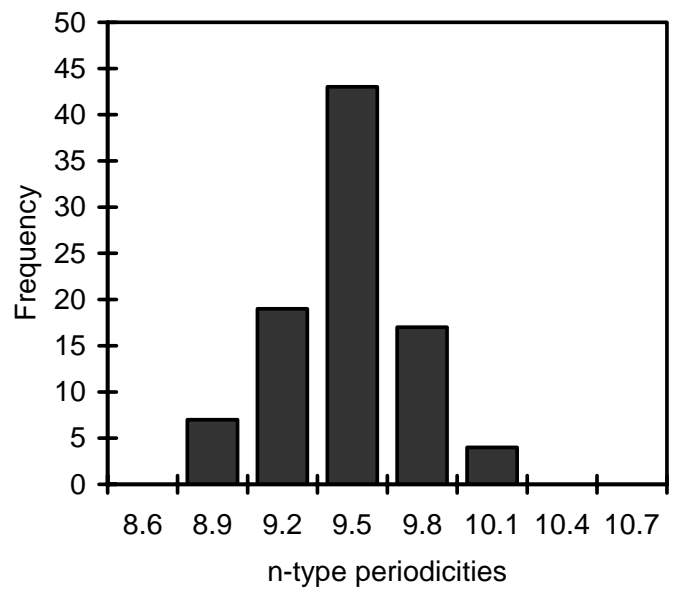
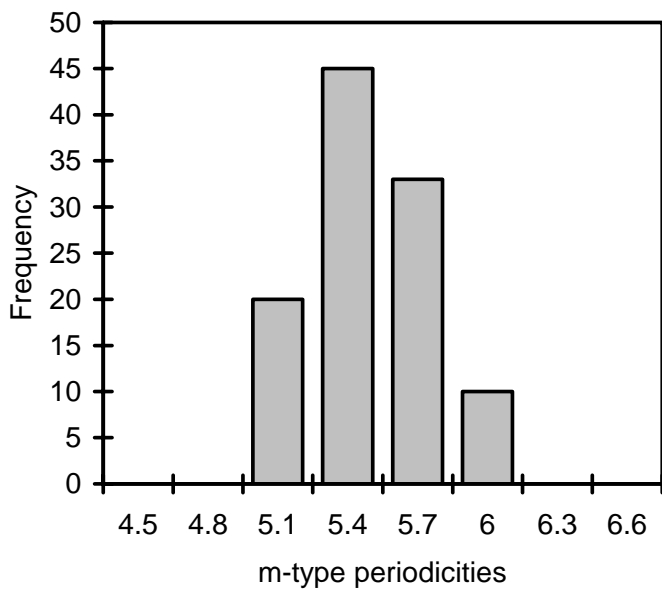
Ferrage et al., Fig. 06



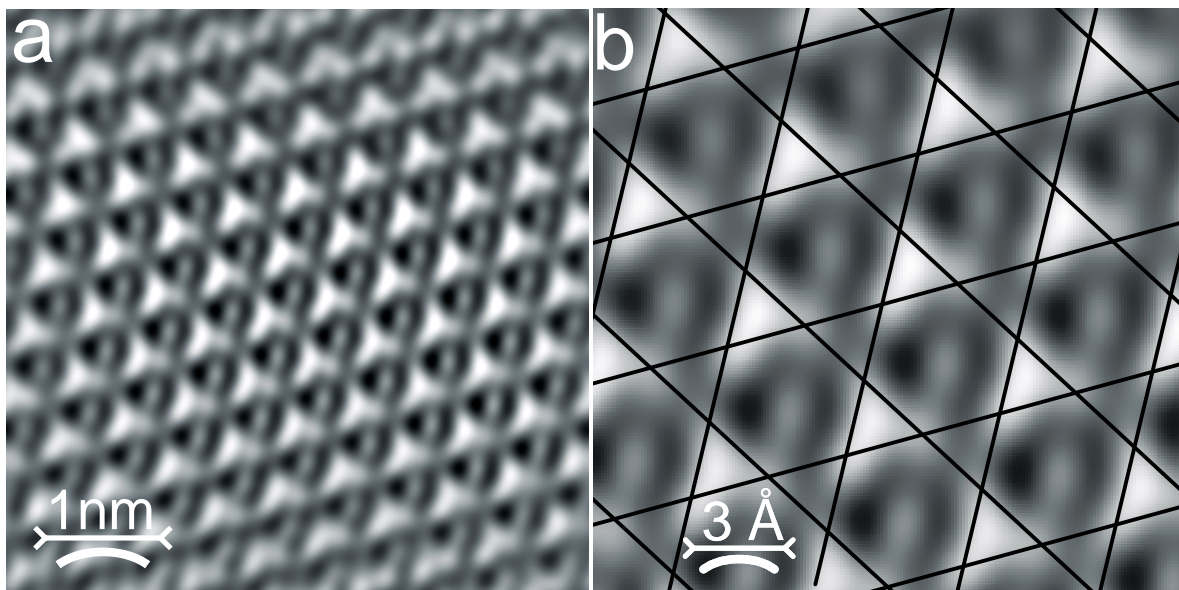
a



Ferrage et al., Fig. 07



Ferrage et al., Fig. 08



Ferrage et al., Fig. 09